



Experimental Study of Shock Oscillation over a Transonic Supercritical Profile

L. Jacquin,* P. Molton,† S. Deck,‡ B. Maury,† and D. Soulevant†
ONERA, 92322 Chatillon, France

DOI: 10.2514/1.30190

Shock wave/turbulent boundary-layer interaction and flow separation may induce self-sustained large-scale oscillations on a profile at transonic Mach number. This phenomenon, known as transonic buffet, is at the origin of intense pressure fluctuations which can have detrimental effects, both in external and internal aerodynamics. The present paper describes a new experiment executed in the ONERA S3Ch transonic wind tunnel on shock oscillations over the OAT15A supercritical profile. These experiments have allowed the precise definition of the conditions for buffet onset and the characterization of the properties of the periodic motion from unsteady surface pressure measurements. The flowfield behavior has been described in great detail thanks to high-speed schlieren cinematography and surveys with a two-component laser Doppler velocimetry along with a conditional sampling technique. The first aim of this study was to provide the computational fluid dynamics community with well-documented test cases to validate advanced computing methods. Concerning the physics of the phenomenon, it is suggested that it is mediated by acoustic waves which are produced at the trailing edge and which travel on the two sides of the airfoil. Also, the experimental results strongly suggest that the phenomenon is essentially two-dimensional, even if three-dimensional effects are also detected.

Nomenclature

c	= airfoil chord length, mm
f	= frequency of unsteady flow oscillation, Hz
f_0	= buffet frequency, Hz
C_p	= mean pressure coefficient, $(p - p_0)/q_0$
$G(f)$	= power spectral density, Pa^2/Hz
M	= Mach number
M_0	= freestream Mach number
N	= number of particles
p	= static pressure, Pa
P_{rms}	= rms value of pressure fluctuations, Pa
p_{st}	= freestream stagnation pressure, Pa
p_0	= freestream static pressure, Pa
q_0	= freestream dynamic pressure, $\rho_0 U_0^2/2$
Re_c	= Reynolds number based on freestream conditions and chord length
R_{nm}	= cross correlation of pressure fluctuation
S_p	= spectrogram of pressure fluctuations
T_{st}	= stagnation temperature, K
U_0	= freestream velocity
$\langle U \rangle$	= longitudinal velocity component, m/s
X, Y, Z	= Cartesian frame
X	= chordwise distance from wing apex, mm
Y	= wing span distance from centerline, mm
Z	= crosswise distance, mm
Z_0	= coordinate of the upper surface, mm
α	= angle of incidence, deg
τ	= time delay, s

I. Introduction

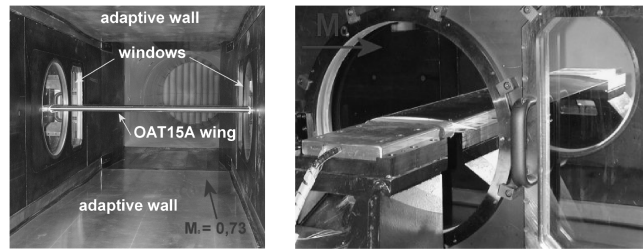
IN TRANSONIC flow conditions, shock wave/turbulent boundary-layer interaction with separation may induce large-scale instabilities involving the whole flowfield and is known as transonic buffet, although buffet is a more general term applying to any flow unsteadiness inducing structural vibrations named buffeting. Transonic buffet is an extremely strong phenomenon which can cause dangerous vibrations leading to the destruction of a wing or a turbomachine blade. Prediction of transonic buffet onset is a problem of outstanding importance for designers because buffet occurrence constitutes an upper bound to the performance of a wing profile in terms of maximum lift or a compressor in terms of pressure ratio. A phenomenon known as buzz, which also concerns shock/flow oscillations, is present in supersonic air intakes where it can be triggered by the interaction of the terminal normal shock with the boundary layer developing inside the air intake [1]. Then, an intense buzz can damage the engine or provokes its extinction. The postponing of buffet onset is a key target in the profile design process and constitutes the aim of most flow control techniques, such as vortex generators on wings or suction slots in air intakes [2]. Experiments [3–6] show that transonic buffet starts when boundary-layer separation takes place at the shock foot and extends down to the profile trailing edge. Then, under particular conditions of Mach number and profile angle of incidence, a large amplitude and periodic motion of the shock can be initiated leading to spectacular oscillations involving the entire flowfield. Capacity of modern computational fluid dynamics (CFD) to predict buffet onset has been investigated by several authors [7–9] and, in general, usual flow models based on the unsteady Reynolds-averaged Navier–Stokes equations (URANS approach) or zonal detached eddy simulation are in measure to predict such flow unsteadiness under conditions which are not yet completely elucidated [10–13]. However, in most applications, agreement with experiment is only qualitative, although the physics of the phenomenon is remarkably simulated by calculation. The aim of the work presented in this paper was to develop an experimental database on transonic buffet to provide well-documented and interpreted cases to validate advanced predictive methods and to improve turbulence models. These experiments were executed in the ONERA S3Ch wind tunnel using a supercritical profile. The database includes high-speed schlieren films, surface oil flow, and sublimating product visualizations, steady and unsteady surface pressure measurements, and phase-averaged laser Doppler velocimetry (LDV) results on the velocity fields.

Presented as Paper 4902 at the 35th AIAA Fluid Dynamics Conference and Exhibit, Toronto, Ontario, Canada, 6 June 2005–9 June 2005; received 1 February 2007; revision received 23 September 2008; accepted for publication 17 November 2008. Copyright © 2008 by the American Institute of Aeronautics and Astronautics, Inc. All rights reserved. Copies of this paper may be made for personal or internal use, on condition that the copier pay the \$10.00 per-copy fee to the Copyright Clearance Center, Inc., 222 Rosewood Drive, Danvers, MA 01923; include the code 0001-1452/09 and \$10.00 in correspondence with the CCC.

*Head Fundamental and Experimental Aerodynamics Department, 29 Avenue de la Division Leclerc, Member AIAA.

†Research Engineer, Fundamental and Experimental Aerodynamics Department, 29 Avenue de la Division Leclerc.

‡Research Engineer, Applied Aerodynamics Department, 29 Avenue de la Division Leclerc.



a) General view

b) Close up of model fixation

Fig. 1 OAT15A supercritical profile in the S3Ch transonic wind tunnel.

II. Experimental Arrangement and Test Conditions

The present study was carried out in the continuous closed-circuit transonic S3Ch wind tunnel of the ONERA-Meudon Center. This facility is powered by a 3500 kW two-stage motor-ventilator group and has a test section size of $0.78 \times 0.78 \times 2.2$ m. The Mach number domain extends from 0.3 to 1.2, the stagnation pressure being the atmospheric pressure, and the stagnation temperature comprised between 290 and 310 K. The upper and lower walls can be either fixed and solid, perforated, or flexible so as to reduce wall interferences near the model, the adaptation technique being based on a steady flow hypothesis [14]. The side walls are equipped with schlieren quality windows. The flow is controlled by a downstream sonic throat which allows setting the test section Mach number with an uncertainty of $\pm 10^{-4}$. The experimental arrangement is shown in Fig. 1.

The model is an OAT15A profile (see Fig. 2a) with a relative thickness of 12.3%, a chord length $c = 230$ mm, a span of 780 mm (which gives an aspect ratio $\mathcal{AR} \approx 3.4$), and a thick trailing edge of 0.5% of the chord length. The central region of the profile is equipped with 68 static pressure orifices and 36 unsteady Kulite pressure transducers. We used two types of Kulite sensors: type XCQL-093-5D (differential, pressure range 0.35 bar, ± 0.35 mbar) and type LQ-24-080-25A [absolute, pressure range 1.710^5 Pa (± 17 mbar)]. Figure 2b shows the location of the orifices and transducers on the profile lower and upper surfaces. The test upstream Mach number M_0 has been varied between 0.70 and 0.75. For the stagnation conditions $p_{st} \approx 10^5$ Pa, $T_{st} \approx 300$ K, the Reynolds number based on the chord length was $Re_c \approx 3 \times 10^6$. The flow incidence α with respect to the profile could be set between 2.5 and 3.91 deg by a proper adjustment

of the adaptive walls, the profile being fixed. The angle of incidence is deduced from the adaptation procedure, preliminary tests with the profile set at different known incidences having validated the method. Boundary-layer transition was triggered on the model by using a carborundum strip located at $X/c = 0.07$ on the upper and lower surfaces.

The experimental program consisted in variation of incidence α for a given Mach number ($M_0 = 0.73$, see Table 1) and of Mach number for two given incidences (see Table 2).

III. Results

A. Flow Visualizations

Sublimating product and surface oil flow visualizations were used to check the quality of the steady flow regime on the profile upper surface. The boundary layer downstream of the carborundum strip is fully turbulent and the separation line at the shock foot is parallel to the leading edge on a large proportion of the profile span. This is illustrated in Figs. 3 and 4 for $\alpha = 2.5$ deg and $M_0 = 0.73$. Figure 3 shows that the sublimating product which initially covers the upper surface of the wing (Fig. 3a) disappears downstream of the tripping line due to the turbulent regime of the boundary layer (Fig. 3b). The oil flow visualization of Fig. 4 reveals that the mean shock remains parallel to the leading edge on nearly 80% of the wing. Flow deviations are apparent in the lateral wall region. These three-dimensional effects which are due to interactions with the side wall boundary layers remain confined to nearly 10% of the profile span at each extremity.

As shown in the next section, buffet onset occurs at incidence $\alpha = 3.1$ deg. A large part of the data described in this paper concerns incidence $\alpha = 3.5$ deg. In this case, buffet is fully established and the shock foot oscillates on nearly 20% of the chord. Oil flow visualization in Fig. 5 shows that, in this case, the mean detachment line remains parallel to the leading edge on a large portion of the wing span. It also reveals the mark of steady vortices in the detached region at the wall, with two symmetric pairs of cells located in the central region of the wing. This 3-D organization of the flow is put in evidence here by penetration of oil products in the central region of the wing, which was not covered initially. The time it takes for this wall flow to establish is several minutes. Schlieren films were recorded for $M_0 = 0.73$, in the range $\alpha = 3$ –3.5 deg (see Table 1) using a high-speed Phantom camera equipped with a 512×512 pixels complementary metal oxide semiconductor sensor allowing acquisitions

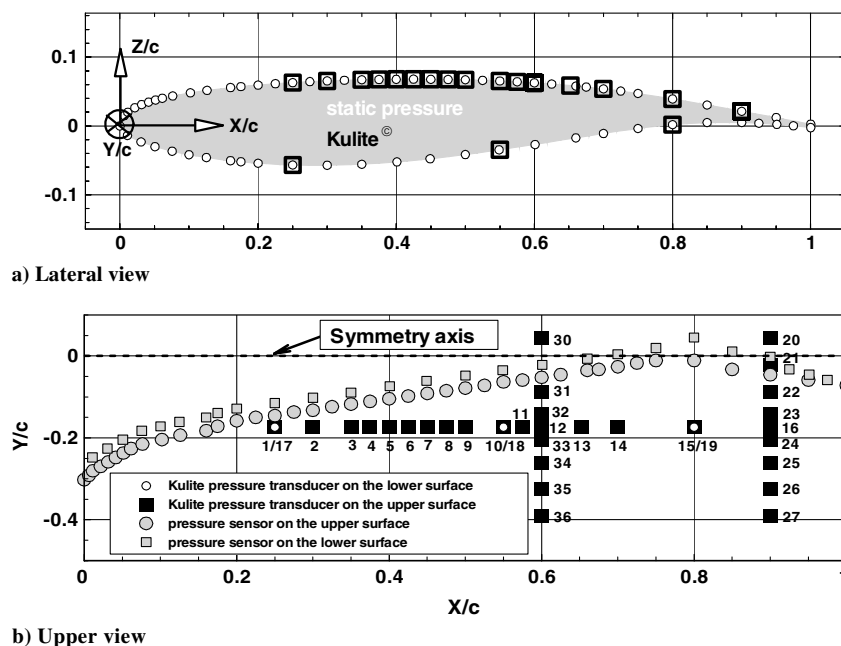


Fig. 2 Locations of the pressure orifices and Kulite transducers.

Table 1 Program chart for $M_0 = 0.73$

α	1.36	1.5	2.5	3	3.05	3.1	3.15	3.2	3.25	3.3	3.35	3.4	3.45	3.5	3.7	3.9
Oil flow			X													
Sublimating product			X													
Steady pressure	X	X	X	X	X	X	X	X	X	X	X	X	X	X		X
Unsteady pressure	X	X	X	X	X	X	X	X	X	X	X	X	X	X	X	X
Schlieren visualization				X	X	X	X	X	X	X	X	X	X	X		

Table 2 Summary table for $\alpha = 3$ and 3.5 deg

M_0	0.71	0.72	0.73	0.74	0.75
Steady pressure	3 deg	3 deg	3 deg	3 deg	3 deg
Unsteady pressure	no	3.5 deg	3.5 deg	3.5 deg	no
Schlieren visualization	no	3.5 deg	3.5 deg	3.5 deg	no



Fig. 3 Sublimating product on the upper surface of the airfoil ($\alpha = 2.5$ deg, $M_0 = 0.73$): a) no flow, b) after sublimation.

of 1000 frames per second. Examples of pictures obtained for $M_0 = 0.73$ and $\alpha = 3.5$ deg are shown in Fig. 6 (these conditions are those of the other investigations presented next). The two pictures correspond to the most upstream and downstream locations of the shock during its oscillation for these conditions. The wave observed upstream of the field is due to the transition triggering strip. Its apparent importance is amplified by the spanwise integration of light deviation which tends to magnify the image contrast. In reality, surface pressure measurements showed that the variations of the flow conditions across this wave were negligible. The photograph in Fig. 6a reveals a lambda-shaped region typical of transonic shock wave/boundary-layer interaction with a shear layer (in white) which develops along the slip line originating from the lambda structure triple point. The separated boundary layer above the profile, behind the shock (in black), is also visible. When the shock wave moves upstream, the shock strength increases (larger Mach numbers) which leads to a larger separation and an increase of the three-dimensional effects at the side walls. Deformations of the shock surface associated with these effects are visible in Fig. 6b.

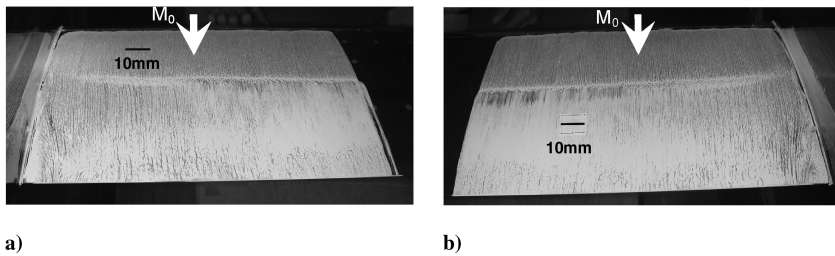


Fig. 4 Oil flow visualization of the upper surface of the wing for $\alpha = 2.5$ deg, $M_0 = 0.73$, viewed from downstream: a) left side, b) right side. The center region of the airfoil is free from oil flow.

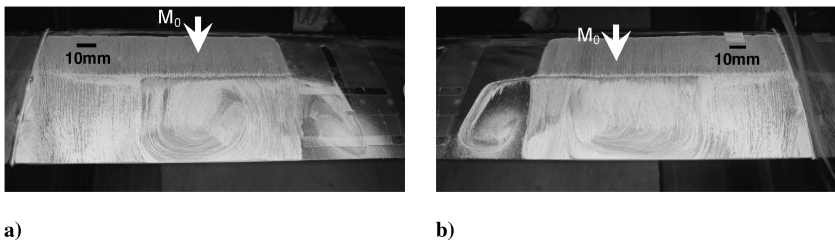


Fig. 5 Oil flow visualization of the upper surface of the wing for $\alpha = 3.5$ deg, $M_0 = 0.73$, viewed from downstream: a) left side, b) right side. The center region of the airfoil is free from oil flow.

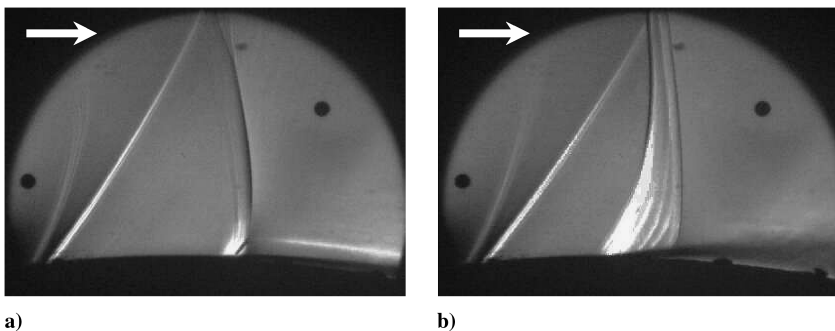


Fig. 6 Instantaneous schlieren pictures for $\alpha = 3.5$ deg, $M_0 = 0.73$: a) shock most upstream location, b) shock most downstream location.

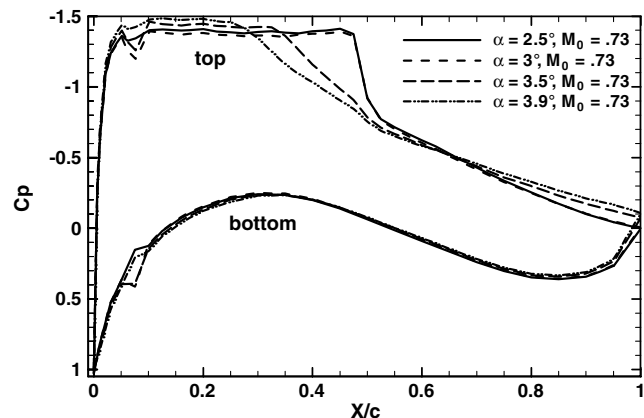


Fig. 7 Mean surface pressure coefficient.

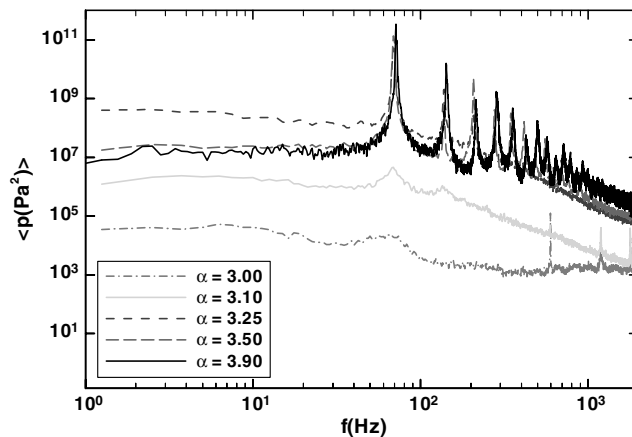


Fig. 10 Influence of incidence on the pressure power spectrum at $X/c = 0.45$ (Kulite no. 7). Upstream Mach number $M_0 = 0.73$.

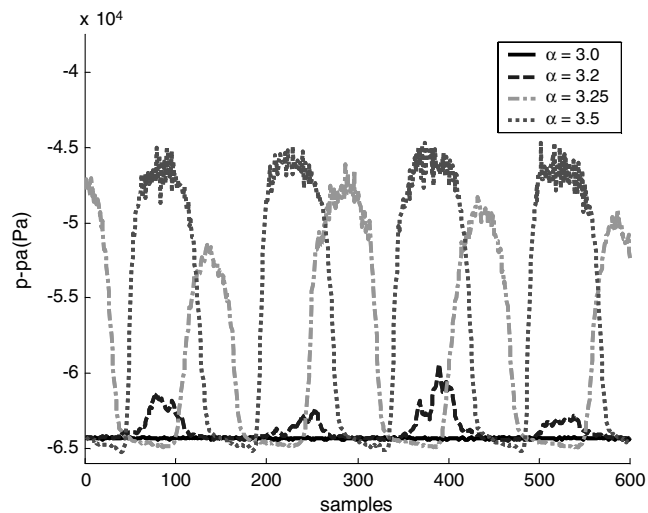


Fig. 8 Time variation of surface pressure signals at $X/c = 0.45$ (Kulite no 7, see Fig. 2b). Upstream Mach number $M_0 = 0.73$.

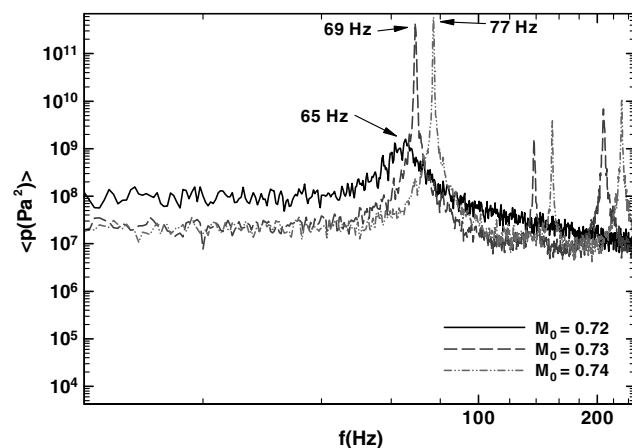


Fig. 11 Influence of Mach number on the pressure power spectrum at $X/c = 0.45$ (Kulite no. 7). Incidence $\alpha = 3.5$ deg.

All these visualizations will be commented on further after presentation of the other measurements.

B. Mean Surface Pressure Measurements

Buffet onset is characterized in Fig. 7 by the distributions of the wall pressure coefficient C_p measured for $M_0 = 0.73$ and four incidence angles ($2.5 < \alpha < 3.9$ deg). The upper curves correspond to the suction side of the airfoil. The lower curves correspond to the pressure side. As shown in the figure, a supercritical profile is

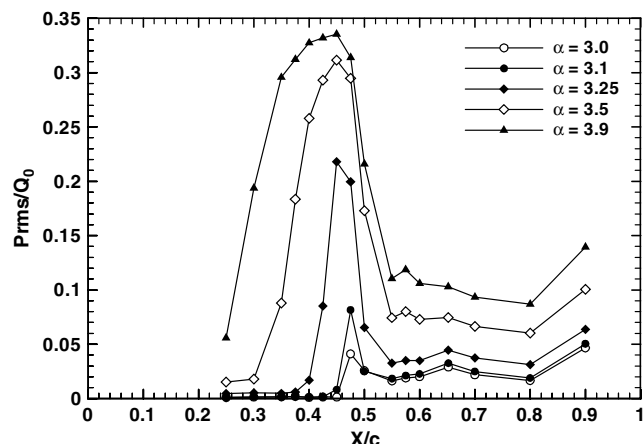


Fig. 9 Influence of incidence on the chord wise distribution of the surface pressure rms. Upstream Mach number $M_0 = 0.73$.

characterized by a pressure plateau (preceding the compression due to the shock) compensated by compression induced by a pronounced camber on the rear part of the airfoil. When $\alpha = 2.5$ and 3 deg, the shock remains steady (no buffet) and is located at $X/c = 0.48$.

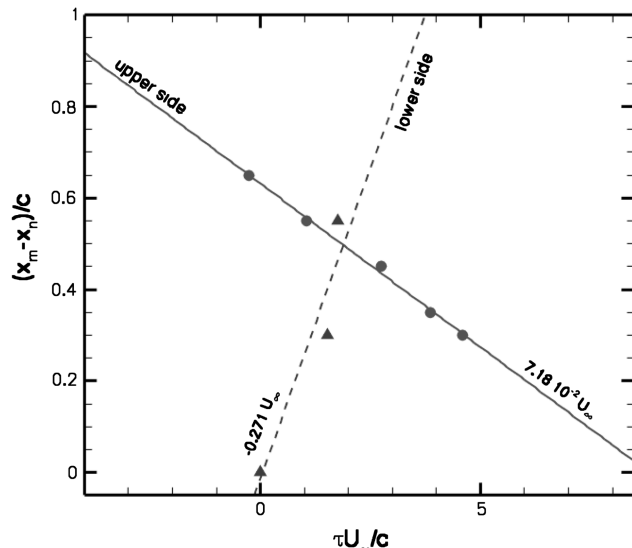


Fig. 12 Maximum values of the space-time correlations of the pressure fluctuations measured on the upstream side of the airfoil behind the shock (circles) and on the lower side (triangles). The convection velocities indicated are obtained by least-square fits. Upstream Mach number $M_0 = 0.73$, angle of incidence $\alpha = 3.5$ deg.

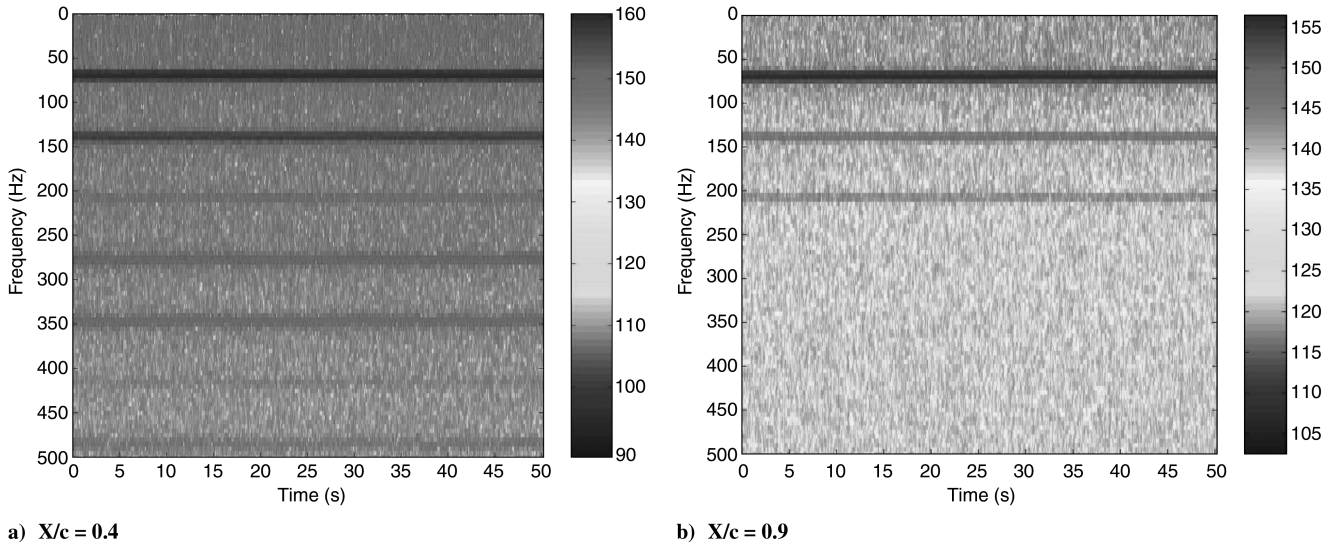


Fig. 13 Spectrograms of the surface pressure fluctuation. Upstream Mach number $M_0 = 0.73$, angle of incidence $\alpha = 3.5$ deg.

The shock starts to oscillate for $\alpha = 3.5$ deg with a maximum upstream excursion detected at $X/c \approx 0.3$ for $\alpha = 3.9$ deg. The spreading of the recompression region in Fig. 7 results from the temporal integration of flow intermittency during shock oscillation. Note also that the thickening of the mean separated region during buffet leads to a pressure decrease at the trailing edge.

C. Unsteady Pressure Coefficients

Both the continuous and fluctuating parts of the pressure signals provided by the Kulite sensors were stored. For the fluctuations, the sampling rate was set to 10240 Hz and low-pass filtered at 4096 Hz. The sample length was fixed to 50 s. As shown in Fig. 7, the most downstream shock position is at $X/c = 0.48$ close to Kulite no. 7 ($X/c = 0.45$; see Fig. 2b). Typical pressure signals delivered by this transducer for four different flow incidences are plotted in Fig. 8. For $\alpha = 3$ deg, the pressure is still steady, perturbation onset being detected for $\alpha = 3.1$ deg. For $\alpha = 3.25$ deg, the pressure signal becomes periodic but its amplitude changes from period to period, indicating that the phenomenon is not yet established. For $\alpha =$

3.5 deg, the sensor is located successively before and behind the shock and the signal is fully periodic. The rms values of the pressure fluctuations on the profile upper surface are plotted in Fig. 9. Before buffet onset ($\alpha = 3$ deg), the fluctuation amplitudes remain weak and localized around $X/c = 0.5$ and 1, that is, at the foot and at the trailing edge. When buffet is established (see $\alpha = 3.25$ – 3.9 deg), strong fluctuations are detected, their maximum being located around $X/c = 0.45$. Then, amplitude and width of the rms distributions increase with the incidence α . Power spectra obtained with the Kulite sensor no. 7 ($X/c = 0.45$) are plotted in Fig. 10 for $\alpha = 3, 3.1, 3.25, 3.5, 3.9$ deg. The frequency resolution was set to 1/3 Hz. For $\alpha = 3$ deg, the shock is stable, the signal energy remaining low and distributed among all frequencies. However, a bump can be detected between 40 and 95 Hz, the amplitude of this bump increasing for $\alpha = 3.1$ deg with a peak emerging at 70 Hz together with its first harmonic. This peak corresponds to the buffet frequency as shown by the curves obtained at higher incidences ($\alpha = 3.25$ and 3.5 deg). Beyond buffet onset, the spectra are marked by high harmonics and by background turbulence. One notes that the energy background overshoots for $\alpha = 3.25$ deg before settling down to a

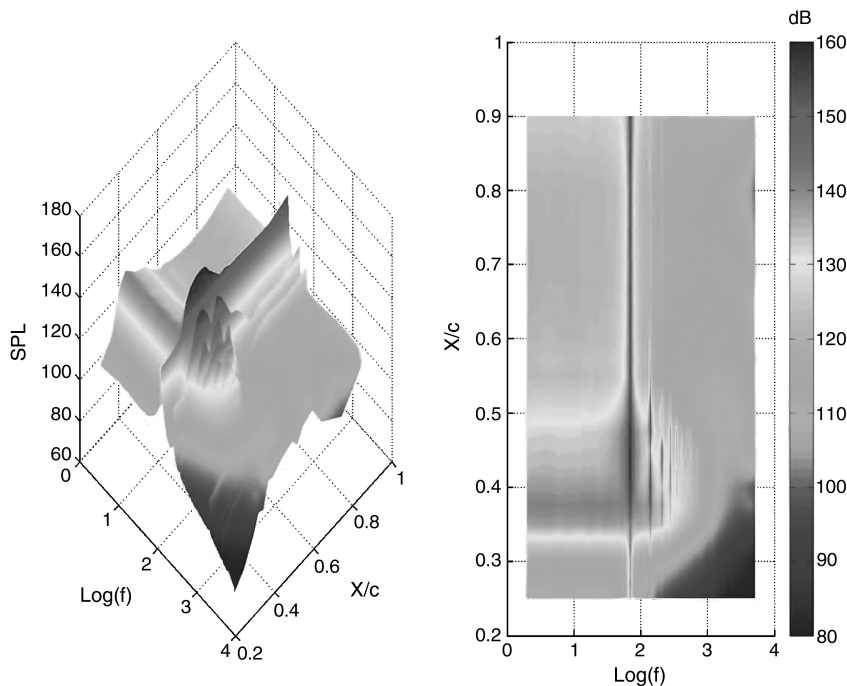


Fig. 14 Distribution of sound pressure levels along the chord on the profile upper surface; left shows 3-D representation, right shows 2-D representation.

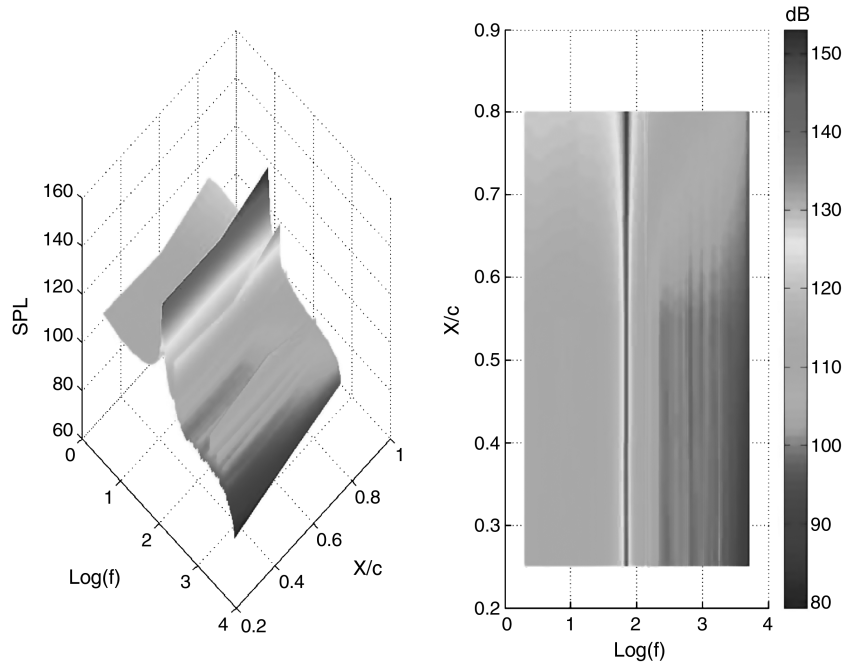


Fig. 15 Distribution of sound pressure levels along the chord on the profile lower surface; left shows 3-D representation, right shows 2-D representation.

lower level for higher incidences. The power spectra curves plotted in Fig. 11 for fixed incidence ($\alpha = 3.5$ deg) and different Mach number show that the buffet frequency increases with M_0 : it emerges at $f_0 = 65$ Hz for $M_0 = 0.72$ and reaches $f_0 = 77$ Hz for $M_0 = 0.74$. These results demonstrate that the buffet phenomenon is sensitive to the upstream Mach number.

D. Cross Correlation of Pressure Fluctuation

The correlation coefficient

$$R_{nm}(\tau) = \frac{\overline{p'_n(t)p'_m(t+\tau)}}{\sqrt{\overline{p_n'^2} \overline{p_m'^2}}} \quad (1)$$

establishes the correlation between two signals ($p'_n(t)$, $p'_m(t+\tau)$) located at abscissas X_n and X_m and separated by a time delay τ .

Convection velocities have been determined from the values of $R_{nm}(\tau)$ calculated on the upper surface using the Kulite transducers located at $X_n/c = 0.25$, $0.55 < X_m/c < 0.9$ and for time delays $|\tau| < 0.1$ s, and on the lower surface using the three available Kulite transducers, cf. Fig. 2. As seen in Fig. 12, one finds on the upper side behind the shock pressure fluctuations propagating downstream with a positive velocity of nearly 17 ms^{-1} ($0.072U_\infty$). On the lower side, acoustics waves travel from the trailing edge toward the leading edge at a speed of nearly -65 ms^{-1} ($-0.27U_\infty$). This is not too far from ($a_\infty - U_\infty$).

E. Spectral Analysis

Figure 13 presents the spectrogram of the pressure fluctuations in the vicinity of the shock and near the trailing edge, respectively. This time-frequency representation of the time-dependent pressure signal is defined by the short-time Fourier transform

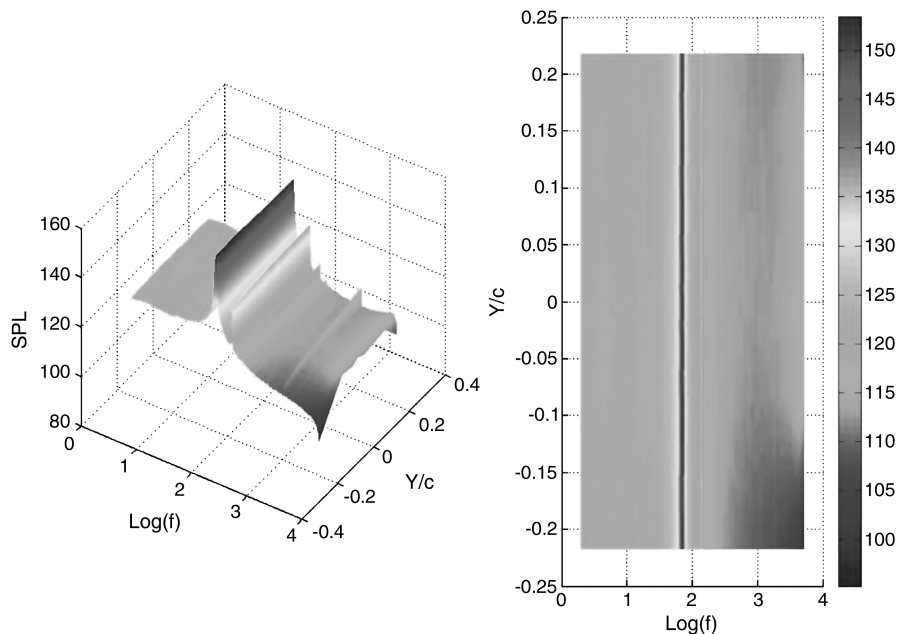


Fig. 16 Spectral surfaces of pressure fluctuation along the spanwise direction at $X/c = 0.6$; left shows 3-D representation, right shows 2-D representation.

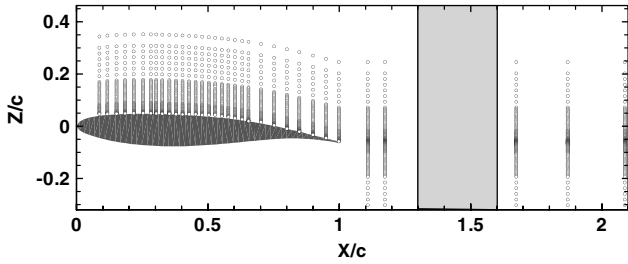


Fig. 17 Mesh definition for the LDV probings.

$$S_p(t, f) = \left| \int_{-\infty}^{+\infty} p(\xi) h(t - \xi) e^{-2\pi i f \xi} d\xi \right|^2 \quad (2)$$

were $h(t)$ is a sliding window. The results plotted in Fig. 13 prove that the spectral composition of the data is time invariant (no mode switching). This holds for the two considered locations, which means that the pressure oscillations remain periodic and correlated over the whole extent of the separation region.

The power spectral density (PSD) can be expressed in terms of sound pressure levels (SPLs) through the relation

$$\text{SPL} = 20 \log_{10} \left(\frac{\sqrt{G(f)}}{2 \times 10^{-5}} \right) \quad (3)$$

where $G(f)$ is the PSD function. The SPLs are mapped in Figs. 14–16. Figures 14 and 15 show the chordwise variations on the profile upper and the lower surface, respectively, and Fig. 16 along a

spanwise direction at $X/c = 0.6$. The three-dimensional maps are plotted on the left and their two-dimensional projection on the right of the figure. Strong harmonic peaks are present, which clearly illustrates the periodic nature of the flow. The peak around 70 Hz is the buffet main frequency. In the intermittent region ($0.35 < X/c < 0.4$), the spectra are dominated by high-amplitude and low-frequency fluctuations. The spreading aspect of the spectra in this region is due to the shock motion. One can also notice the enrichment of the spectra with regards to higher frequencies at further downstream locations toward the profile trailing edge. Figure 15 shows that the spectral signature of the shock motion near 70 Hz is also detected on the profile lower surface. In Fig. 16, one can notice that the spectral content does not change in the spanwise direction at a given abscissa, so that the data can be considered as two-dimensional from a spectral point of view in the midspan section.

F. Velocity Field Measurements

The velocity field for $M_0 = 0.73$ and $\alpha = 3.5$ deg has been probed by means of a two-component LDV system (measuring the longitudinal component u and the vertical component w of the velocity) operating in the forward scattering mode and equipped with an IFA750 signal processor of TSI, Inc. A Bragg cell unit was used to produce a frequency shift of 40 MHz, thus allowing measurements in separated flow regions. The radius of the probe volume was estimated to be ≈ 0.27 mm and the length of its major axis (in the spanwise direction) to 5 mm. Approach to the walls was limited to 0.3 mm in most cases (0.2 mm sometimes). The flow was seeded with DEHS (Di-Ethyl-Hexyl-Sebacat) submicronic droplets introduced upstream of the profile, in the wind-tunnel settling chamber. Bias due

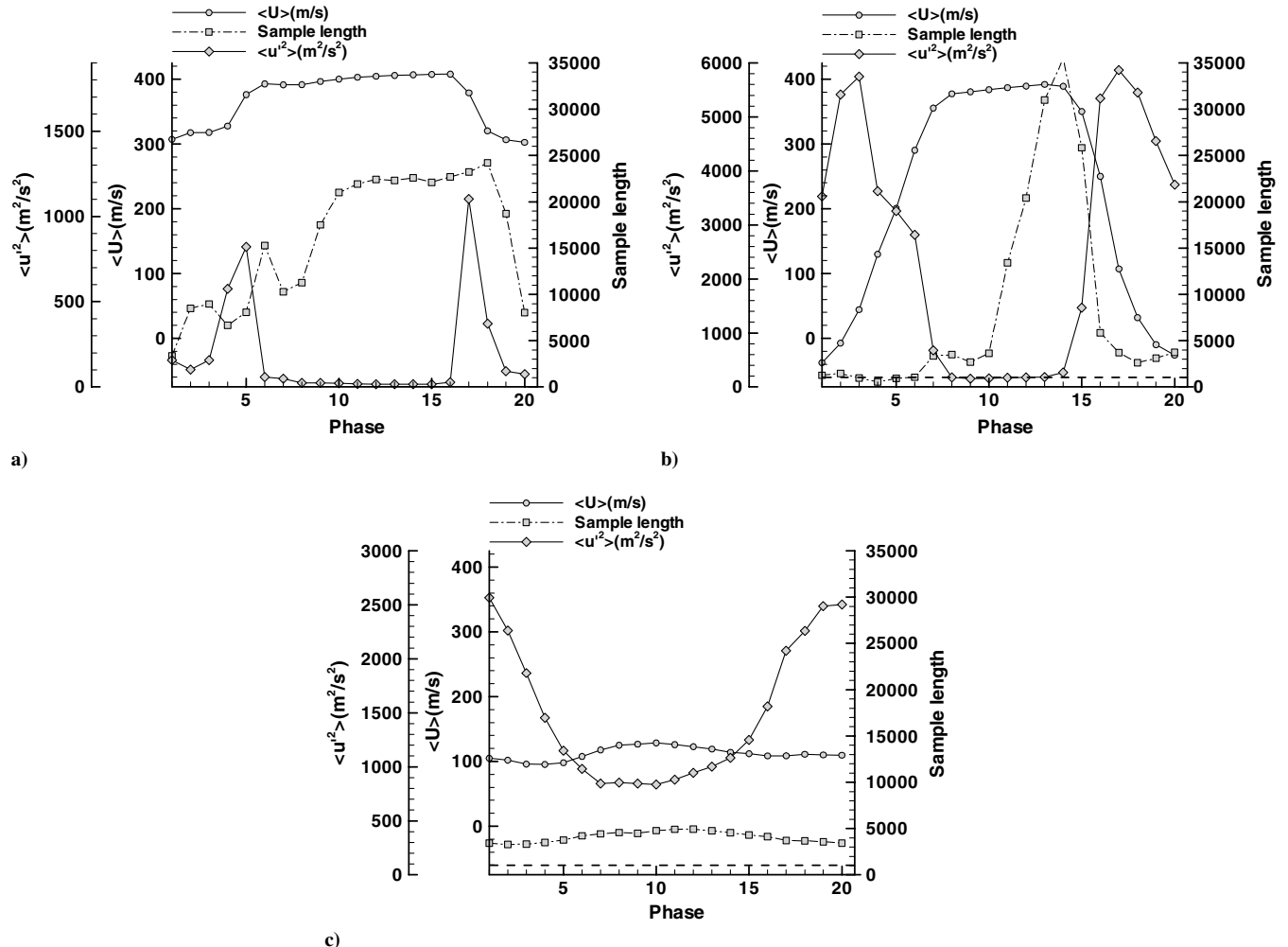


Fig. 18 Conditional analysis of LDV results. Phase average of the longitudinal velocity component (U), rms of the longitudinal velocity fluctuation (u^2), number of particles N : a) $X/c = 0.48, z/c = 0.12$, b) $X/c = 0.48, z/c = 0.04$, c) $X/c = 1.1, z/c = 0.06$.

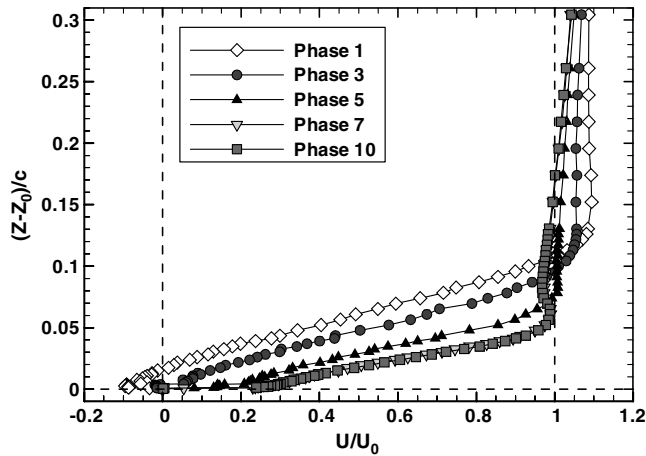


Fig. 19 Phase-averaged streamwise velocity profile at $X/c = 1$.

to particle inertia are negligible in the shear layers of transonic flows for such particles (see Forestier et al. [15]). They may become more important in the shock region. But for the present flow conditions, this should remain confined within a typical distance of order 1 mm behind the shock. A typical data rate of 20 kHz was achieved in the freestream. The measured level of turbulence in the freestream was about 1%, which corresponds in fact to the typical noise level of standard LDV systems. The exploration mesh, shown in Fig. 17, consisted of a series of vertical lines located at the spanwise location $Y/c = -0.43$ with, on each of these lines, measuring points distributed according to a spacing varying from $\Delta z = 0.2$ to $\Delta z = 2$ mm (the total number of points was equal to 2174). The shaded region corresponds to the separation between the two windows visible in Fig. 1b where no measurements were possible.

Phase averages were determined using the pressure signal measured by the Kulite transducer no. 7, which is located close to the mean shock location. The following data processing was then performed: 1) acquisition of LDV signals synchronized with the pressure signal, 2) determination of the flow period from the low-pass filtered pressure signal, 3) segmentation of the period into 20 bins in which data is stored, 4) computation of ensemble averages in each

bin of the velocity (phase averages) and of the moments of the differences with respect to this phase averages (random fluctuations). This leads to the classical triple decomposition:

$$\underline{u}(\underline{x}, t) = \bar{u}(\underline{x}) + \tilde{u}(\underline{x}, t) + \underline{u}'(\underline{x}, t) \quad (4)$$

where $\bar{u}(\underline{x})$ denotes the ensemble average of the statistically steady variable $\underline{u}(\underline{x}, t)$, $\tilde{u}(\underline{x}, t)$ being its cyclic component and $\underline{u}'(\underline{x}, t)$ the random component. The phase-averaged velocity is defined as $\langle \underline{u} \rangle(\underline{x}, t) = \bar{u}(\underline{x}) + \tilde{u}(\underline{x}, t)$. This procedure is detailed in Forestier et al. [15] where it was applied to a transonic mixing layer over a resonant cavity. The results are illustrated in Fig. 18, which shows, for three typical locations in the field, the phase average of the axial velocity, the rms values of the random part of this velocity component, and the number of particles used for these calculations. The minimum sample length (number of particles) needed for a reasonable convergence of the rms values $\langle u'^2 \rangle$ and $\langle w'^2 \rangle$ is set to 1000. The first measurement point (Fig. 18a) is located outside the boundary layer, at the mean shock location. The second one (Fig. 18b) is in the lambda region of the mean shock. Both the mean velocity and data rate depend here on the shock position with respect to the measurement point. The rms values sharply increase when the shock crosses the LDV probe volume. The third point (Fig. 18c) is located in the profile wake, the results showing that the separation induced by shock oscillation leads to significant variations in the rms values in the wake. Note also the strong variations of the sample rate with the phase, especially in Fig. 18b. This may introduce important velocity bias errors on Reynolds-averaged quantities deduced from standard ensemble averages (higher velocities contribute more). Here, this bias can be eliminated by reducing the length of all the bins to a constant value chosen as the minimum value among the 20 bins. The averages among the 20 bins having the same sample length become free from velocity bias, see Forestier et al. [15].

Profiles of the velocity phase average measured above the profile trailing edge are plotted in Fig. 19. These profiles show that buffet leads to periodic separation and attachment of the boundary layer in conjunction with the shock motion: the boundary layer is separated when the shock is in the upstream location (phase 1) and attached when it moves downstream. Figure 20 shows maps of the phase-averaged longitudinal velocity component, deduced from LDV measurements, corresponding to four successive positions of the

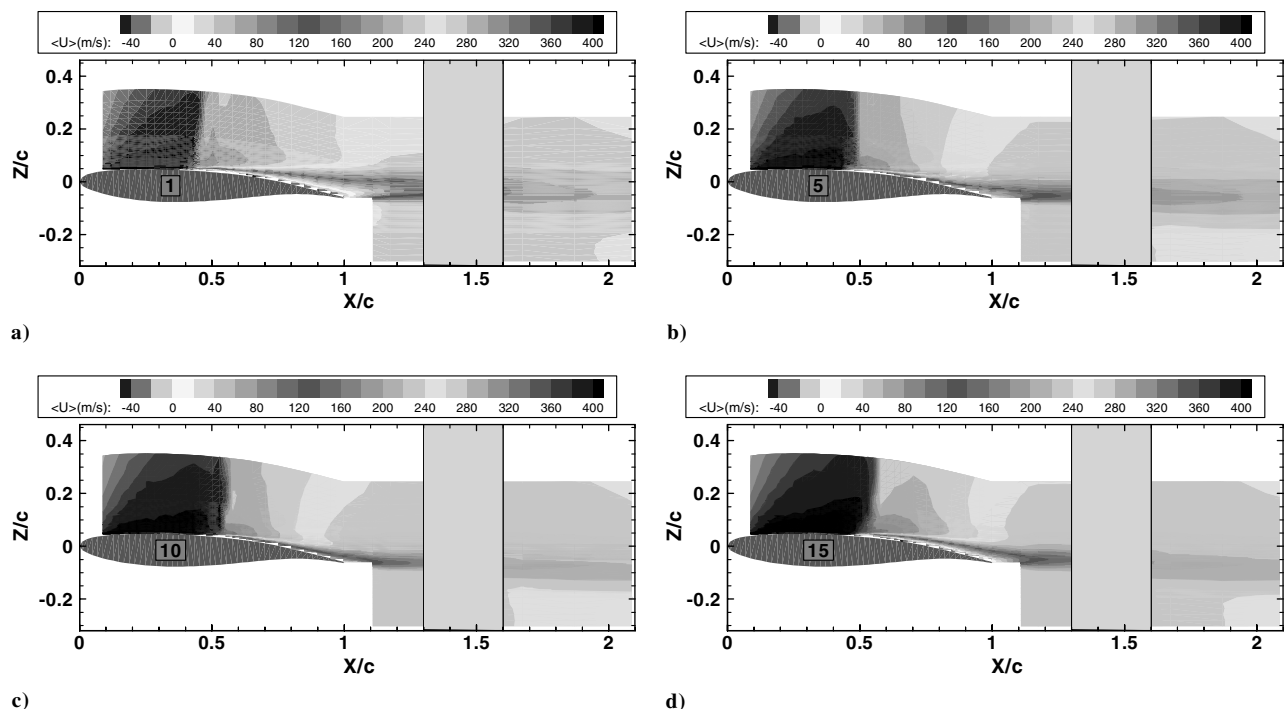


Fig. 20 Phase-averaged longitudinal velocity: a) with shock upstream (phase 1), b) with shock during its downstream travel (phase 5), c) with shock downstream (phase 10), d) with shock during its upstream travel (phase 15).

shock during its periodic motion. In the first picture (see Fig. 20a), the shock occupies its most upstream position and, in this case, the boundary layer is separated from the shock foot down to the profile trailing edge. The second picture (see Fig. 20b), corresponds to an intermediate position of the shock during its downstream travel. During this displacement, the boundary layer undergoes a substantial thickening because of the shock destabilizing effect and of the adverse pressure gradient on the profile rear part. However, the boundary layer remains attached, except maybe in a small region at the trailing edge. When the shock is at its most downstream location (see Fig. 20c), there is an important thickening of the boundary layer as if the shock then induces separation. During the forward motion (see Fig. 20d), the size of the separated region steadily grows and extends from the shock foot to the trailing edge. Separation will suddenly disappear as the shock stops before starting to move in the downstream direction again.

IV. Discussion

The usefulness of the present databank for validation of numerical tools has already been comforted by several successful CFD works based on our results [11–13,16]. Hopefully, the present data also provides some novel insights in the physics of buffet. First, the conditional analysis of the velocity fields described earlier, see Figs. 18–20, confirms that buffet is characterized by a coupled modulation of the shock wave movement and the separation of the boundary layer. The spectral analyses of pressure signals and the success of the phase-averaging procedure applied to the velocity field confirm that the mechanism is essentially modal. In a recent publication, Crouch et al. [17] considered the linearized RANS equations and demonstrated that buffet onset corresponds to destabilization of a single global mode. These authors used the data of McDevitt and Okuno [18] to test their stability theory (see Crouch et al. [17]). They also used our data to extend their conclusions to the case of a modern supercritical profile (see Crouch et al. [16]). In this latter paper, the periodic components of the velocity $\tilde{u}(x, z)$ and $\tilde{w}(x, z)$ determined by our conditional LDV measurements were compared, quite successfully, to the global velocity mode provided by stability analysis of a steady RANS field validated with the present data. Now, some physical interpretations of the phenomenon may be investigated a little by searching model expressions of the selected buffet frequency. Considering $f \approx 70$ Hz as the buffet-onset frequency and using the airfoil chord c and the freestream velocity $U_\infty = 241$ m/s to normalize this frequency, one gets $S = fc/U_\infty \approx 0.067$. McDevitt and Okuno [18] obtained $S \approx 0.045$ on the NACA0012 airfoil. Lee [6] obtained $S \approx 0.081$ on a supercritical airfoil.

A physical interpretation of the global mechanism characterized by the stability analysis of Crouch et al. [16,17] may be tried considering an acoustic feedback loop composed by hydrodynamic instability waves convecting over the upper side toward the trailing edge, where they generate acoustic waves propagating upstream toward the shock location from which further instability waves are generated. Acoustic waves may hit the shock from behind after propagation above the upper surface of the wing. But they can also impact the shock from upstream after traveling along the lower surface and after turning round the leading edge. We saw that the signals delivered by the three Kulite sensors located on the lower surface confirmed the presence of such traveling waves below the airfoil, see Fig. 12; this was also observed in the pressure global mode described by Crouch et al. [16,17].

Semi-empirical modeling, which could predict this buffet frequency f , can then be proposed, given a physical model of the self-sustained shock wave oscillation caused by such an acoustic feedback loop. Following a classical approach for such a model, one may consider that the time scale $1/f$ is equal to the sum of different characteristic time scales. A first one is the time $\tau_c = l_u/U_c$ it takes for instability waves induced by the shock oscillations to reach the trailing edge. Here, $l_u \approx c/2$ the mean shock/trailing edge distance and U_c denotes the propagation speed of the instability waves. A second time scale is an acoustic time scale. Two possibilities may be considered: $\tau_{a,u} = l_u/U_{a,u}$, which characterizes propagation of

acoustic waves of celerity $-U_{a,u}$ traveling backward toward the shock above the upper side of the airfoil, and $\tau_{a,l} = l_l/U_{a,l}$, which characterizes propagation of acoustic waves below the lower surface from the trailing edge to the leading edge. Here $l_l = c$. These last waves hit the shock from upstream after turning round the leading edge and after fast convection in the supersonic region ahead of the shock. Neglecting the time taken for these two last phases of the process and supposing that the characteristic propagation velocity below the airfoil remains close to $-U_{a,u}$, one gets $\tau_{a,l} \approx 2\tau_{a,u}$.

Difficulties come from evaluation of the propagation velocities. In particular, the propagation speed U_c is unknown. From Fig. 12, we obtained $U_c \approx 0.072U_\infty$. This characterizes perturbations propagating from the shock foot toward the trailing edge at a low celerity. By following the same approach as that described here, Lee [6] also considered for U_c the phase of pressure fluctuation signals delivered by unsteady pressure sensors. He obtained values of U_c which are comparable to that obtained in Fig. 12. Interpretation of these traveling pressure waves is difficult and it seems that no simplified expression can easily model this part of the global phenomenon. Note that a very different value for U_c could be retained if adopting a local stability point of view where U_c is considered as the convection speed of Kelvin—Helmholtz-type perturbations traveling along the detached flow mixing layer. Such a scenario would suggest to take for U_c a value close to $U_c \approx U_\infty/2$ (if considering that the velocity behind the shock remains on average close to U_∞), namely, an estimation an order of magnitude larger than that of the perturbation velocity which dominates the correlations (see Fig. 12). Estimation of the acoustic velocities $U_{a,u}$ and $U_{a,l}$ is easier, a crude estimation being $(a_\infty - U_\infty)$ which gives $(U_\infty(1 - M_\infty)/M_\infty = 0.37U_\infty)$ for $M_\infty = 0.73$ (this could be refined to separate the region behind the shock on the upper side from that on the lower side). This leads to an expression of the frequency under the form $f = (\tau_c + \tau_a)^{-1}$ with $\tau_c \approx 6.7610^{-3}$ s and where τ_a can be taken as $\tau_{a,u} \approx 1.2810^{-3}$ s, $\tau_{a,l} \approx 2.5510^{-3}$ s, or as a sum of these two time scales. This frequency is mainly determined here by the smaller time scale, that is, the convection time scale τ_c of the instability waves, a parameter which is unfortunately difficult to model. Ignoring the acoustic contributions would lead to $f = 1/\tau_c \approx 147$ Hz. Adding the two time scales, $\tau_a = \tau_{a,u} + \tau_{a,l}$, provides at most a decrease of the selected frequency down to $f \approx 94$ Hz. This is still too high, but acceptable. Indeed, refinements of such a crude model could be attempted, but this is not our purpose here. The preceding analysis mainly shows that the reduction of the global physics of the buffet to a simple scheme is not easy. The main hypothesis the preceding reasoning is based on is that buffeting is driven by two cooperating mechanisms: the convection of instability perturbations generated at the shock foot, a region which is viewed as a receptivity one, forced by a feedback from acoustic propagation. However, expressions for the different time scales involved, especially that of the downstream convection of instability perturbations in the detached region, are lacking.

Now, the 2-D nature of the mechanism is a second matter of concern. Several facts support the idea that buffet flow is essentially 2-D. First, models based on steady or unsteady Reynolds-averaged Navier-Stokes equations (RANS [16,17] and URANS [10,11,13] approaches) have successfully reproduced the main characteristics of buffeting flows on airfoils. This is a first indication in favor of a 2-D mechanism. In the experiment, the accumulation line at the shock foot in the oil flow visualizations of Figs. 4 and 5 do not show any well-defined 3-D deformation of the shock surface (except in the lateral wall regions). Moreover, we saw in Fig. 16 that the pressure data in the central part of the wing could be considered as two-dimensional from a spectral point of view. However, when the buffet amplitude increases, oil flow visualizations provide clear indications that the mean wall flowfield is not strictly 2-D anymore in the separated region (see Fig. 5).

These are apparently conflicting results. However, note that quite different quantities are characterized by the pressure taps and by the oil-film flow: the pressure is produced by the Euler flow above the viscous layers and is of order ρU_0^2 , whereas the oil-film gives insights into the wall velocity field which is an order of magnitude lower than

U_0 (away from shock regions). This means that velocity associated with the 3-D patterns in Fig. 5 is small compared to the longitudinal velocity above the detached flow. In terms of origin, these conflicting observations may be, for instance, reconciled by considering that they originate from stiff 2-D pressure waves produced by a more 3-D hydrodynamic organization in the separated flow. It is interesting to note that similar 3-D patterns have already been observed in detached flows over airfoils. For instance, Schewe [19] made oil-film flow visualizations over the airfoil of a wind powerplant of aspect ratio $AR = 4$ at an angle of attack of 12 deg and found, at $Re = 1.2 \times 10^6$, a double pair of mushroomlike structures in the separated flow similar in shape to those shown in Fig. 5. In this case, this 3-D flow organization seems to be triggered by the laminar/turbulent transition and to depend on its location on the airfoil [19], and it characterizes an intermediate state between attached flow ($Re = 0.8 \times 10^6$, maximum lift) and fully detached flow ($Re = 7.4 \times 10^6$, lower lift). In our case, such structures develop in a fully turbulent regime and they survive to the periodic reattachment/detachment of the buffet flow (sweeping of the separation region during the attached flow phases may explain why the structures in Fig. 5 are blurred). These remarks thus suggest that such a 3-D mechanism could be universally related to the transition process toward massive flow separation. A picture based on the superposition of a strong 2-D global mode with a weaker 3-D could for instance be admissible. One could also envisage a spanwise variation of the initially 2-D global mode which characterizes onset, when the airfoil incidence is increased above its critical value. However, another possible cause may be effects of the lateral walls. For instance, the URANS simulations by Thiery and Coustols [13] have shown a periodic development of such 3-D structures when the lateral walls are included in the computation domain. Anyhow, all these elements remain speculative and more theoretical, and experimental works are still needed for catching the right physics of this flow.

V. Conclusions

Flow unsteadiness triggered by shock-induced separation over a supercritical transonic profile (the ONERA OAT15A profile) has been experimentally investigated in great detail to provide well-documented test cases to validate advanced predictive methods. The data also provide new information that can help improve understanding of the phenomenon. The study was executed in a transonic wind tunnel equipped with adaptive walls for several upstream Mach numbers and angles of incidence to precisely characterize the conditions leading to transonic buffet. The flow was investigated by means of surface flow visualization, high-speed schlieren cinematography, steady and unsteady surface pressure measurements, and flowfield surveys by a two-component LDV system. The pressure data have provided a precise definition of the conditions for buffet onset as a function of the flow upstream Mach number and profile incidence. The periodic oscillation of the velocity field over the profile and in its wake has been quantified by means of conditional processing of LDV measurements. These results are consistent with the classical scenario for the transonic buffet process which involves the shock motion and the boundary-layer behavior in a periodic and closely coupled interaction. During the downstream displacement of the shock, the boundary layer remains attached over nearly all the profile chord; then, separation at the shock foot takes place when the shock is stopped in its most downstream location. During the shock forward motion, the separation region grows in size until it extends down to the profile trailing edge when the shock reaches its most upstream position. When the shock stops again in its most upstream location, separation at the shock foot disappears and a new cycle starts with a boundary layer attached. The physics of buffet has been further discussed by considering the scaling of the buffet frequency and the 2-D/3-D nature of the detached buffeting flow. A heuristic approach based on the principle of hydrodynamic/acoustic resonance has been explored. The spatiotemporal properties of the phenomenon, investigated by means of pressure data spectral analysis, show that the mechanism is nearly two-dimensional and periodic. Other evidences that dynamics of buffet must be mainly

two-dimensional and periodic are mentioned. However, wall flow visualizations reveal the development of 3-D patterns restricted to the separated flow region. As discussed in the last section, these findings cannot yet be concealed and call for further explorations of these flow physics.

Acknowledgments

The authors gratefully acknowledge the Service des programmes Aéronautiques from the French Ministry of Defense which granted the research reported in this paper. They are also thankful to the editor and to the reviewer who clearly helped to make this paper better than it was initially.

References

- [1] Seddon, J., and Goldsmith, E. L., *Intake Aerodynamics*, W. Collins, London, 1985.
- [2] Caruana, D., Mignosi, A., Corrège, M., and Le Pourhiet, A., "Buffeting Active Control in Transonic Flow," AIAA Paper 2003-3667, June 2003.
- [3] Finke, K., "Unsteady Shock-Wave Boundary-Layer Interaction on Profiles in Transonic Flow," AGARD-CP-168, Paper 28, 1975.
- [4] Seegmiller, H. L., Marvin, J. G., and Levy, L. L., "Steady and Unsteady Transonic Flow," *AIAA Journal*, Vol. 16, No. 12, 1978, pp. 1262–1270. doi:10.2514/3.61042
- [5] Levy, L. L., "Experimental and Computational Steady and Unsteady Transonic Flows About a Thick Airfoil," *AIAA Journal*, Vol. 16, No. 6, 1978, pp. 564–572. doi:10.2514/3.60935
- [6] Lee, B. H. K., "Transonic Buffet on a Supercritical Aerofoil," *Aeronautical Journal*, May 1990, pp. 143–152.
- [7] Rubesin, M. W., Okuno, A. F., Levy, L. L., McDevitt, J. B., and Seegmiller, H. L., "An Experimental and Computational Investigation of the Flow Field About a Transonic Airfoil in Supercritical Flow with Turbulent Boundary-Layer Separation," *10th Congress of the International Council of the Aeronautical Sciences*, Oct. 1976.
- [8] Lazaref, M., and Le Balleur, J. C., "Calcul des écoulements Visqueux Tridimensionnels sur les ailes Transsoniques par Interaction Fluide Parfait/Couche Limite," *La Recherche Aérospatiale*, No. 1983-3, 1983.
- [9] Bartels, R. E., "Computation of Shock Buffet for Conventional and Supercritical Airfoil," AIAA Paper 97-833, Jan. 1997.
- [10] Chung, I., Lee, D., and Reu, T., "Prediction of Transonic Buffet Onset for an Airfoil with Shock Induced Separation Bubble Using Steady Navier-Stokes Solver," AIAA Paper 2002-2934, June 2002.
- [11] Brunet, V., "Computational Study of Buffet Phenomenon with Unsteady RANS Equations," AIAA Paper 2003-3679, June 2003.
- [12] Deck, S., "Numerical Simulation of Transonic Buffet ONERA Supercritical Airfoil," *AIAA Journal*, Vol. 43, No. 7, 2005, pp. 1556–1566. doi:10.2514/1.9885
- [13] Thiery, M., and Coustols, E., "Numerical Prediction of Shock Induced Oscillations over a 2D Airfoil: Influence of Turbulence Modelling and Test Section Walls," *International Journal of Heat and Fluid Flow*, Vol. 27, 2006, pp. 661–670.
- [14] Le Sant, Y., and Bouvier, F., "A New Adaptive Test Section at ONERA Chalais-Meudon," *European Forum on Wind Tunnels and Wind Tunnel Test Techniques*, Southampton Univ., Southampton, England, U.K., Sept. 1992.
- [15] Forestier, N., Jacquin, L., and Geffroy, P., "The Mixing Layer over a Deep Cavity in a Transonic Regime," *Journal of Fluid Mechanics*, Vol. 475, 2003, pp. 101–145. doi:10.1017/S0022112002002537
- [16] Crouch, J. D., Garbaruk, A., Magidov, D., and Jacquin, L., "Global Structure of Buffeting Flow on Transonic Airfoils," *Proceedings of the IUTAM Symposium*, Vol. 14, 2009 (to be published).
- [17] Crouch, J. D., Garbaruk, A., and Magidov, D., "Predicting the Onset of Flow Unsteadiness Based on Global Instability," *Journal of Computational Physics*, Vol. 224, No. 2, 2007, pp. 924–940. doi:10.1016/j.jcp.2006.10.035
- [18] McDevitt, J. B., and Okuno, A. F., "Static and Dynamic Pressure Measurements on a NACA0012 Airfoil in the Ames High Reynolds Number Facility," NASA Tech. Paper No. 2485, 1985.
- [19] Schewe, G., "Reynolds-Number Effects in Flow Around More-or-Less Bluff Bodies," *Journal of Fluids Engineering and Industrial Aerodynamics*, Vol. 89, 2001, pp. 1267–1289.